CAMBRIDGE
UNIVERSITY PRESS

Check for updates

Research Article

Evolutionary map of the universe (EMU): Observations of filamentary structures in the Abell S1136 galaxy cluster

Peter J. Macgregor[1,2], Ray P. Norris[1,2], Andrew O'Brien[1,2], Mohammad Akhlaghi[3], Craig Anderson[2,4], Jordan D. Collier[1,2,5], Evan J. Crawford[6], Stefan W. Duchesne[7,8], Miroslav D. Filipović[1], Bärbel S. Koribalski[1,2], Florian Pacaud[9], Thomas H. Reiprich[9], Christopher J. Riseley[8,10,11], Lawrence Rudnick[12], Tessa Vernstrom[8,13], Andrew M. Hopkins[14], Melanie Johnston-Hollitt[15], Josh Marvil[4], Matthew Whiting[2] and Steven Tingay[7]

[1]School of Science, Western Sydney University, Locked Bag 1797, Penrith, NSW, 2751, Australia, [2]Australia Telescope National Facility, CSIRO, Space and Astronomy, PO Box 76, Epping, NSW 1710, Australia, [3]Centro de Estudios de Física del Cosmos de Aragón (CEFCA), Unidad Asociada al CSIC, Plaza San Juan 1, 44001 Teruel, Spain, [4]National Radio Astronomy Observatory, PO Box 0, Socorro, NM87801, USA, [5]The Inter-University Institute for Data Intensive Astronomy (IDIA), Department of Astronomy, University of Cape Town, Private Bag X3, Rondebosch, 7701, South Africa, [6]School of Computer, Data, and Mathematical Sciences, Western Sydney University, Locked Bag 1797, Penrith, NSW, 2751, Australia, [7]International Centre for Radio Astronomy Research (ICRAR), Curtin University, Bentley, WA 6102, Australia, [8]Australia Telescope National Facility, CSIRO, Space and Astronomy, PO Box 1130, Bentley, WA 6151, Australia, [9]Argelander-Institut für Astronomie, Universtät Bonn, Auf dem Hügel 71, 53121, Bonn, Germany, [10]Dipartimento di Fisica e Astronomia, Università degli Studi di Bologna, via P. Gobetti 93/2, 40129 Bologna, Italy, [11]INAF – Istituto di Radioastronomia, via P. Gobetti 101, 40129 Bologna, Italy, [12]University of Minnesota, Minnesota Institute for Astrophysics, 116 Church St. SE, Minneapolis, MN 55455 USA, [13]ICRAR, The University of Western Australia, 35 Stirling Hw, 6009 Crawley, Australia, [14]Australian Astronomical Optics, Macquarie University, 105 Delhi Rd, North Ryde, NSW 2113, Australia and [15]Curtin Institute for Data Science, Curtin University, Perth, GPO Box U1987, WA 6845, Australia

Abstract

We present radio observations of the galaxy cluster Abell S1136 at 888 MHz, using the Australian Square Kilometre Array Pathfinder radio telescope, as part of the Evolutionary Map of the Universe Early Science program. We compare these findings with data from the Murchison Widefield Array, XMM-Newton, the Wide-field Infrared Survey Explorer, the Digitised Sky Survey, and the Australia Telescope Compact Array. Our analysis shows the X-ray and radio emission in Abell S1136 are closely aligned and centered on the Brightest Cluster Galaxy, while the X-ray temperature profile shows a relaxed cluster with no evidence of a cool core. We find that the diffuse radio emission in the centre of the cluster shows more structure than seen in previous low-resolution observations of this source, which appeared formerly as an amorphous radio blob, similar in appearance to a radio halo; our observations show the diffuse emission in the Abell S1136 galaxy cluster contains three narrow filamentary structures visible at 888 MHz, between ∼80 and 140 kpc in length; however, the properties of the diffuse emission do not fully match that of a radio (mini-)halo or (fossil) tailed radio source.

Keywords: galaxies: clusters: individual: (Abell S1136); radio continuum: galaxies

(Received 24 October 2022; revised 8 April 2024; accepted 21 April 2024)

1. Introduction

Galaxy clusters are large gravitationally-bound structures, containing hundreds to thousands of galaxies, with typical masses of 10^{14} to 10^{15} M$_\odot$. Approximately 80% of this mass is Dark Matter, $15-17\%$ is the intra-cluster medium (ICM), and only $3-5\%$ is the galaxies that make up the cluster (Feretti et al., 2012). The ICM consists of heated gas situated between the galaxies, including hot X-ray emitting gas at temperatures of 10^7-10^8 K (Ghirardini et al., 2019). Galaxy clusters have also been inferred to have magnetic fields of the order of 0.1 to 1 µG (e.g. Clarke et al.,

2001; Carilli & Taylor, 2002; Bonafede et al., 2010; Donnert et al., 2018).

Diffuse radio emission is often observed in clusters (van Weeren et al., 2019; Paul et al., 2023) and is generated by synchrotron radiation, indicating the presence of relativistic particles and magnetic fields (van Weeren et al., 2016; Hurley-Walker et al., 2021). Because the synchrotron emitting electrons have a limited lifetime, the relativistic particles must either be re-accelerated or created in place (Jaffe, 1977; Filipović & Tothill, 2021).

The spectral energy distribution of the synchrotron radio emission is a function of the ages of the electron populations, the strength of the magnetic fields, and the possible shock-driven re-acceleration from merger events (Feretti et al., 2012; Bonafede et al., 2014; Hurley-Walker et al., 2021).

The radio emission from galaxy clusters can be broadly classified into four categories, depending on the location, morphology, and polarisation properties (see van Weeren et al., 2019, for a recent review): (a) radio emission from the constituent galaxies,

including bent-tail galaxies; (b) diffuse halos of radio emission (radio halos) broadly positioned on the centre of the cluster; (c) diffuse elongated radio shocks typically found on the periphery of the cluster; and (d) fossil radio galaxies.

Radio halos are sources of diffuse radio emission, which are thought to occur more frequently in clusters linked with merger activity, and are associated with the centre of the merging galaxy clusters (Brunetti et al., 2009; van Weeren et al., 2016). The halo spans the region where most of the X-ray emission from the ICM is observed, with recent energy injection into the ICM and corresponding high X-ray temperature and luminosity (e.g. Giovannini et al., 1999; Cuciti et al., 2021a,b; Paul et al., 2023; Tümer et al., 2023).

Radio halos have traditionally been categorised into two classes based primarily on their sizes: giant radio halos (or just 'radio halos') with a typical linear size of ~ 1 Mpc, and mini-halos which typically have a size of less than 500 kpc. Radio halos have a low surface brightness and a steep radio spectrum, with typical integrated spectral indices of $-1.4 < \alpha < -1.1$[a].

Other important distinctions between mini-halos and giant radio halos include the fact that mini-halos are almost exclusively found in cool-core clusters (van Weeren et al., 2019), with the mini-halo centered on the radio-loud Brightest Cluster Galaxy (BCG). Gitti et al. (2015) show the size of the mini-halo is comparable to that of the central cooling region in the cluster, although recent results with the SKA Pathfinders and Precursors (e.g. Riseley et al., 2022a; Biava et al., 2024) show diffuse synchrotron emission from mini-halos outside this central cooling region. In addition, Cassano et al. (2008) found that regardless of the origin of the emitting electrons, even though radio halos and mini-halos have similar radio power, a mini-halo radius is typically ~ 4 times smaller than a radio halo; implying an ~ 50 times larger synchrotron emissivity for the mini-halo; however, some studies (e.g. Riseley et al., 2022a, 2023) show larger sizes in high sensitivity data, with mini-halos often on size scales comparable to "normal" radio halos.

Botteon et al. (2022) note the difficulty of using a scale size to distinguish between 'normal' radio halos and mini-halos, given the wide range of cluster masses, so do not distinguish between a mini-halo and a radio halo. As detailed above, recent high sensitivity observations also show ambiguity in the ability to distinguish between these sources based on size. Similarly, we do not make this distinction.

Radio shocks (a.k.a. 'relics' or 'gischts') are regions of elongated, diffuse emission that do not have an optical counterpart; typically found around the periphery of a cluster. Their radio spectrum is typically a steep power-law, with spectral indices in the range $-1.5 < \alpha < -1.0$, indicating electron cooling in the post-shock region of a shock wave travelling outward (e.g. Giacintucci et al., 2008; van Weeren et al., 2010, 2011; Stroe et al., 2014; Hindson et al., 2014; Riseley et al., 2022b). Radio shocks have been found to be polarised at the level of $\sim 10 - 60\%$ above 1 GHz in merging galaxy clusters (e.g. Ensslin et al., 1998; Giovannini & Feretti, 2004; van Weeren et al., 2010; Rajpurohit et al., 2022). They exhibit strong depolarisation at frequencies < 1 GHz (Brentjens, 2008; Pizzo, 2011; Ozawa et al., 2015).

[a]We adopt the convention that the spectral index α is defined by $S_\nu \propto \nu^\alpha$, where S_ν is the flux density and ν is the frequency.

Fossil radio galaxies (sometimes known as 'phoenices' or 'revived fossil plasma' (Kempner et al., 2004), and confusingly, occasionally as 'relics'), are the remains of dead radio-loud active galactic nuclei (AGN) in which radio plasma from previous AGN activity is compressed by a shock wave. The shock increases both the magnetic field strength inside the plasma and the energy of the plasma particles, resulting in an increase in synchrotron emission. Compared with radio shocks, these sources are generally found at smaller cluster-centric distances (Feretti et al., 2012) and have sizes ranging from $\lesssim 100$ kpc as seen in Abell 2063 and Abell 4038, up to ~ 350 kpc as seen in Abell 85. The emission in many cases has a steep curved spectrum (e.g. Riseley et al., 2022b; Rudnick et al., 2022a; Slee et al., 2001; Venturi et al., 2017), typically steeper than $\alpha \sim -1.5$, characteristic of an old population of electrons. The remnant is found close to the source galaxy, in the inner tens of kpc from the galaxy cluster. When observed with sufficient angular resolution (Slee et al., 2001) the sources are often filamentary.

In recent years there has been a dramatic increase in the discovery of ICM filaments associated with radio galaxies and galaxy clusters, thanks to high-resolution low frequency sub-GHz observations with new generation telescopes such as the Australian Square Kilometre Array Pathfinder (ASKAP), MeerKAT, and the Low Frequency Array (LOFAR) (e.g. Pasini et al., 2022; Rudnick et al., 2022a; Velović et al., 2023).

Abell S1136 is located in the Pisces-Cetus supercluster, at RA(J2000) $= 23^h36^m17.0^s$ DEC(J2000) $= -31°36'37''$, and was first observed as part of the Abell Catalogue 'Southern Survey' in 1988 (Olowin, 1988). It is reported in the Meta-Catalogue of X-ray Detected Clusters of Galaxies as MCXC J2336.2-3136 (Piffaretti et al., 2011) with luminosity $L_{500} = 0.50 \times 10^{37}$ W and mass $M_{X,500} = 1.29 \times 10^{14}$ M$_\odot$ within an $R_{500} = 0.75$ Mpc radius. The Abell S1136 cluster has a spectroscopic redshift of $z = 0.0622$ (De Propris et al., 2002; Campusano et al., 2018) on the BCG ESO 470–20 (Lauberts & Valentijn, 1989).

Observations with the Murchison Widefield Array (MWA; Tingay et al., 2013; Bowman et al., 2013) at 168 MHz (Offringa et al., 2016; Duchesne et al., 2021) found Abell S1136 to host steep-spectrum, diffuse emission (Duchesne et al., 2021, their section 3.2.21). The observed features of the emission were consistent with a number of cluster radio sources including radio halos, radio relics, and remnant radio galaxies. There is no corresponding 1400 MHz or 843 MHz emission seen in the NRAO VLA Sky Survey (NVSS) (Condon et al., 1998) or the Sydney University Molonglo Sky Survey (SUMSS) (Bock et al., 1999; Mauch et al., 2003), implying a steep spectral index.

We present observations of Abell S1136 using the ASKAP (Johnston et al., 2007, 2008; McConnell et al., 2016; Hotan et al., 2021), as part of the Early Science program of the Evolutionary Map of the Universe (EMU) survey (Norris et al., 2011). Section 2 describes the observations, which were taken to investigate the structure of the diffuse radio emission centered on the Abell S1136 galaxy cluster. In Section 3 we present our results, while in Section 4 we discuss the intra-cluster filamentary structure discovered in the Abell S1136 galaxy cluster, and the implications of these results.

This paper assumes a flat ΛCDM cosmology with $H_0 = 68$ km s^{-1} Mpc^{-1}, $\Omega_m = 0.3$, and $\Omega_\Lambda = 0.7$. Using these cosmological parameters, this gives a scale of 1.234 kpc arcsec^{-1} at a redshift of $z = 0.0622$ (the preferred redshift of Abell S1136).

Table 1. Observation and image details of the ASKAP data.

Pointing Centre RA (J2000)	$23^h\ 36^m\ 17.00^s$
Pointing Centre DEC (J2000)	$-31°34'37''$
Scheduling Block ID	9164
Antennas	33
Antenna Numbers	1, 2, 3, 4, 5, 6, 7, 8
	9, 11, 12, 13, 14,15,16
	17, 18, 19, 20, 21, 22
	24, 25, 26, 27, 28, 29
	31, 32, 33, 34, 35, 36
Centre Frequency (MHz)	888
Bandwidth (MHz)	288
Channels	288
RMS (μJy/beam)	
robust $= 0.0$	~ 40
robust $= +2.0$	~ 110
PAF Beams	36
Beam ($''\times''$)	
robust $= 0.0$	12.60×10.04
robust $= +2.0$	25.51×21.27
Footprint	closepack36
Duration (hr)	10.05

2. Observations

2.1. ASKAP observations

We observed Abell S1136 on 29th July 2019 with the ASKAP, as part of the EMU Early Science Broadband (700-1800 MHz) Survey, under Project Code AS034 (Table 1). The observation used a 33 antenna array with a maximum baseline of 6 km. We used a centre frequency of 888 MHz, and the full instantaneous bandwidth of 288 MHz available at the time, divided into 288×1-MHz channels.

Only 33 of the 36 ASKAP antenna were available for this observation. For this observation the 36 Phased Array Feed (PAF) beams on each antenna were set at a pitch of 0.90 degrees with a 45-degree rotation, and formed into a 'closepack36' footprint which provides uniform sensitivity without interleaving (Norris et al., 2021).

The resulting synthesised beam is $12.6'' \times 10.1''$ at 888 MHz for robust $= 0$ weighting. The observation was performed as a single field with 10 hours on source. PKS 1934−638 was used as the primary and secondary calibrator, to provide bandpass and gain calibration for imaging. Data calibration and imaging were performed using the ASKAPsoft (Guzman et al., 2019) data processing pipeline, running at the Pawsey Supercomputing Centre. We produced two sets of images: one at robust $= 0$ weighting (Briggs, 1995), and the other at robust $= +2.0$ (Table 1).

As a check on amplitude calibration across the 888 MHz ASKAP observing tile, we cross-matched the ASKAP data with the 887.5 MHz Rapid ASKAP Continuum Survey (RACS) (McConnell et al., 2020) data. We identified 15 unresolved point sources in and around the Abell S1136 cluster, and measured their flux densities in the ASKAP and RACS data using the Cube Analysis and

Table 2. Observation and image details of the MWA 2 and Australia Telescope Compact Array (ATCA) data.

Band	ν_c	t_{obs}	σ_{rms}	Beam
(MHz)	(MHz)	(min)	(mJy beam^{-1})	($''\times''$)
MWA 2				
72−103	88	62	8.6	128×126
103−134	118	64	4.4	95.6×94.3
139−170	154	78	2.6	74.0×72.8
170−200	185	78	2.4	62.5×61.6
200−231	216	60	4.5	53.9×53.7
ATCA				
1076−3124	2100	1207	0.012	6.31×3.05

Rendering Tool for Astronomy[b] (CARTA; Comrie et al., 2021). The flux densities are in good agreement, with an average Mean Absolute Deviation error of 5.81%.

2.2. MWA observations

We observed Abell S1136 with the Murchison Widefield Array (MWA; Tingay et al., 2013) Phase 2 in its 'extended' configuration (hereafter MWA 2; Wayth et al., 2018; Beardsley et al., 2019), for the MWA project G0045 (PI Duchesne). This observation was to perform a follow-up survey of the diffuse, non-thermal galaxy cluster emission originally detected by the MWA in its Phase 1. The MWA 2 data cover 72−231 MHz, with five 30 MHz observing bands centred on 88 MHz, 118 MHz, 154 MHz, 185 MHz, and 215 MHz. The observing strategy and data reduction process is described in detail by Duchesne et al. (2020). We used robust $= 0$ weighting and present the observation and image details in Table 2.

2.3. Australia telescope compact array observations

We observed Abell S1136 with the Australia Telescope Compact Array (ATCA; Frater et al., 1992; Nelson, 1992; Wilson et al., 2011) over two sessions and using two compatible array configurations[c], at 1100−3100 MHz (the weighted central frequency after the removal of radio frequency interference is 2120 MHz). The first observation was with a 6A array on the 29th April 2016 (PI Duchesne) under project code CX356. This array consists of baselines ranging from 337 m to 6 km, with only 3 of the 15 baselines shorter than 1087 m (337 m, 628 m, and 872 m). The second observation was on 15th November 2020 (PI Macgregor) using a 6B array, under project code CX476. This array consists of baselines ranging from 214 m to 6 km, with only 4 of the 15 baselines shorter than 1270 m (214 m, 536 m, 750 m, and 949 m). This gives a predicted RMS (1σ) noise level for a 12 hour observation of $9\ \mu$Jy beam^{-1} which is close to what we measure in our image as $1\sigma = 12\ \mu$Jy beam^{-1}.

The data were calibrated using MIRIAD (Sault et al., 1995). The primary calibrator for each observation was PKS 1934−638, and gain calibrators PKS 2313−340 (CX356) and PKS 2337−334 (CX476). We imaged the observation using MFCLEAN, with the bandwidth left at 2000 MHz, and robust $= 0$. Three rounds

[b]https://cartavis.org/
[c]https://www.narrabri.atnf.csiro.au/operations/array_configurations/configurations.html

of phase-only self-calibration were performed, and images were cleaned using MFCLEAN down to 3 times the RMS noise. The ATCA observation and image details are shown in Table 2.

The primary beam of the ATCA at 2100 MHz centre frequency is 23.1′ Full Width at Half-Maximum (FWHM), which is comparable with the size of the images shown in this paper. The Compact Array Broadband Backend (CABB) (Wilson et al., 2011) provides a 2 GHz bandwidth when observing at 2100 MHz; this gives a FWHM of 45.07′ at 3214 MHz, and a 15.52′ FWHM at 1076 MHz. Although the ATCA data are corrected for the primary beam shape, the flux densities of sources far (i.e. $\gtrsim 11.5'$ radius/23′ diameter) from the pointing centre (at RA(J2000) = 23$^{\rm h}$ 36$^{\rm m}$ 17.23$^{\rm s}$ DEC(J2000) = $-31°$ 36′ 14.″22, which is close to the BCG), may be unreliable as, at points beyond the FWHM the effective observing frequency varies with distance from the pointing centre (Thompson et al., 2017), and the errors on the flux estimates become larger.

Additionally, as the ATCA observations had limited short spacing information, they were insensitive to the extended diffuse emission; so we do not attempt to derive spectral indices of the diffuse emission from the ATCA data, but use the ATCA observations only for compact sources and narrow filaments.

3. Results

3.1. Filamentary structures

With the higher sensitivity and resolution of the ASKAP data, the steep-spectrum and diffuse cluster emission previously identified by Duchesne et al. (2021), can be seen in Figure 1(a) and (b) to break up into several more compact structures. Radio continuum emission detected in these images are divided into regions of diffuse emission with filamentary structure. We identify three filamentary structures:

1. The 'Northern Filament', which appears to extend north-east from WISEA J233615.95−313534.4, the source labelled 'A'. This filament is ∼ 140 kpc in length (assuming a distance to Abell S1136 of 250 Mpc), and appears detached from source A.
2. The 'BCG Filament', which appears to extend south-east from WISEA J233616.55−313609.3/ESO 470−20, which is the Abell S1136 Brightest Cluster Galaxy (Lauberts & Valentijn, 1989) labelled 'B'. This filament is ∼ 140 kpc long, and appears to be in projection, or to be attached to, source 'B'.
3. The 'Southern Filament', which appears to extend nearly horizontally under WISEA J233616.10−313741.1, the source labelled 'C'. The filament appears to be oriented tangentially to the cluster. This filament is the shortest at ∼ 80 kpc in length.

Sources A and B are cluster radio galaxies, while C is a likely background source, as described below.

Figure 1(a) shows that the Abell S1136 galaxy cluster has multiple AGN located near the centre, with a radio-loud BCG. In Figure 1(b), the large-scale diffuse radio emission is largely symmetric around the BCG, with a morphology that resembles a Wide-Angle-Tail (WAT) source. However, Figure 1(a) shows that the high-resolution image does not resemble a WAT, in that it consists of two relatively straight filaments that do not curve towards each other, unlike the jets of most WATs. Furthermore, the northern filament is not connected to the BCG filament or to the BCG. It might be argued that the low-resolution 154 MHz image in

Figure 2(c) shows two radio lobes, but at higher resolution (e.g. Figure 2(f)) these break up into a combination of diffuse emission and compact sources, in which the filaments do not point to the patches of diffuse emission. Therefore, while we cannot rule out that the Northern and BCG filaments are sections of a WAT associated with the BCG, this would be a very unusual WAT.

3.2. Abell S1136 flux density measurements

We imaged the Abell S1136 galaxy cluster and its filamentary and diffuse components (see Table 3) using data from the MWA Phase II at 154 MHz, 185 MHz, and 216 MHz, ASKAP at 888 MHz and ATCA at 2100 MHz, as shown in Figure 2.

For each of the diffuse regions and filaments measured in the ASKAP image, we used NoiseChisel (see below) to measure the integrated flux density of the same regions in the ATCA data at 2100 MHz, after images were regridded and convolved to the ASKAP beam size using MIRIAD (Sault et al., 1995).

3.2.1. Properties of the diffuse emission and filaments

To detect and measure diffuse emission, we used the NOISECHISEL[d] and MAKECATALOG tools, which are part of the GNU Astronomy Utilities (Gnuastro; Akhlaghi & Ichikawa, 2015; Akhlaghi, 2019b). NoiseChisel uses very low thresholds to nonparametrically detect extended regions of elevated brightness, to very low signal-to-noise (S/N) ratios (Akhlaghi, 2019a).

To measure the uncertainty of this integrated flux density, we used MakeCatalog's –UPPERLIMIT: the footprint of the region was randomly placed in parts of the image with similar noise properties[e], discarding any position where the displaced footprint overlaps with a detection, and the sum of pixel values was measured. The process was terminated after 10 000 successful measurements (–UPNUM=10 000). The sigma-clipped median (m_r) and standard deviation (σ_r) of this random distribution were calculated and compared with the total sum within the region (s), giving an estimate of significance of $(s - m_r)/\sigma_r$.

Figure 2(a) shows the NoiseChisel detection of diffuse emission in Abell S1136 as the green-shaded pixels. Figure 2(b) shows other likely detections in the image at the same level, as black pixels, showing that similar extended regions of diffuse emission are not found elsewhere in the image.

Using the 888 MHz ASKAP robust = 0 image, shown in Figure 2(a), we used NoiseChisel to measure the flux density of the three filaments above a surface brightness threshold of 100 μJy beam^{-1} (shown as a purple outline in the green emission in Figure 2(a)). Similarly, we measured the flux density of the diffuse emission (shown in green) using only NoiseChisel-detected pixels above this threshold. The results are listed in Table 3. In each case, uncertainties were estimated as described above.

Using the uncertainty estimation technique described above, we obtain a significance for this detection of 9.7σ. To confirm that this high fraction is not due to a concentrated region (that may have been missed in the masking) and is mostly uniform, we manually divided the diffuse region into two, shown as blue and red in

---

[d]The following NoiseChisel options were changed compared to the default (using Gnuastro version 0.15): because radio data are already heavily smoothed, convolution was disabled with –KERNEL=NONE, the quantile-threshold was increased with –QTHRESH=0.5 and the growth-threshold was decreased to –DETGROWQUANT=0.85. Furthermore, to increase purity, we used –SNQUANT=0.999.

[e]The input images in all bands are much larger than the small crop shown in Figure 2, allowing good sampling over the noise.
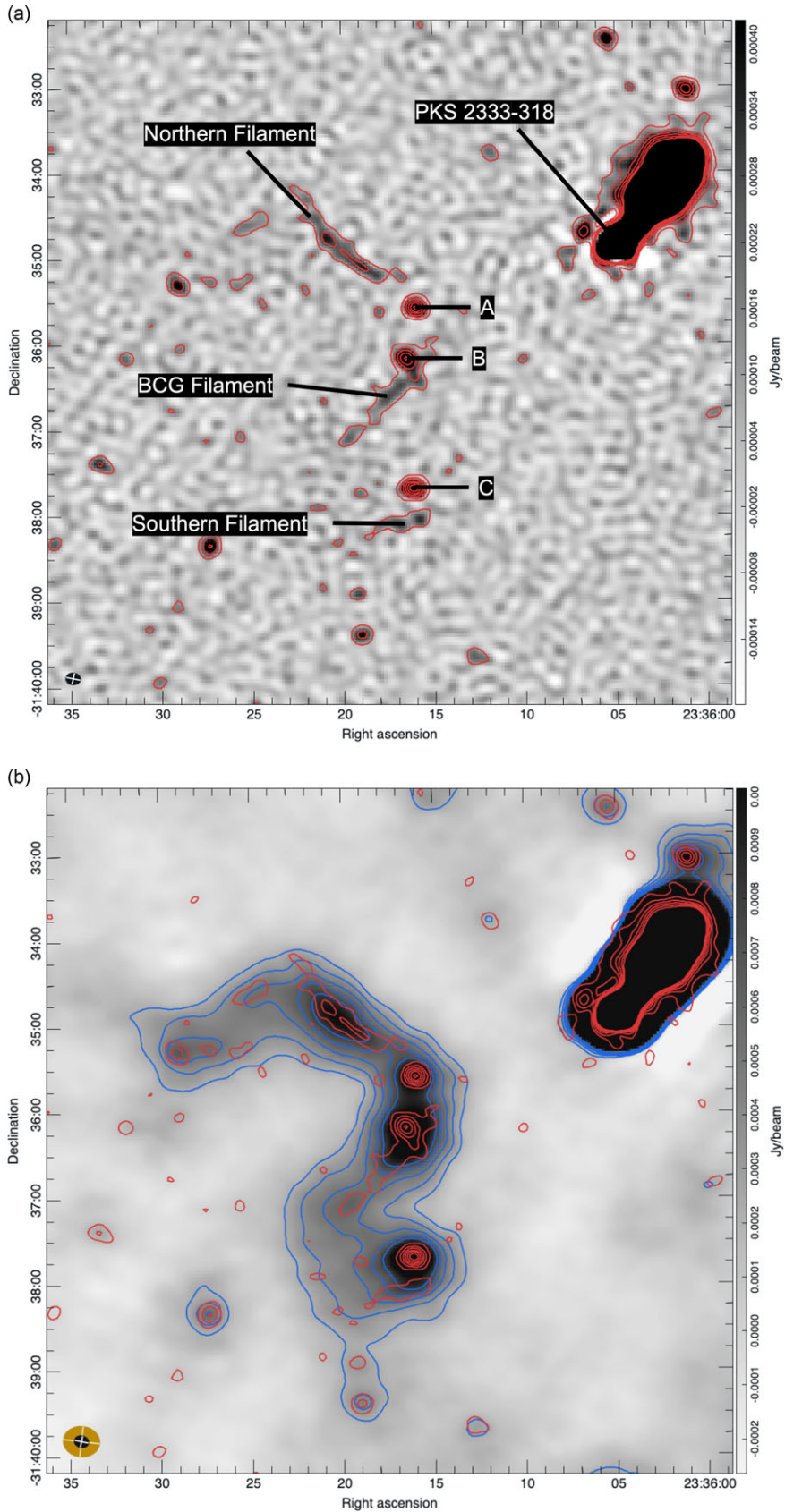
Figure 1. ASKAP 888 MHz radio continuum images of the galaxy cluster Abell S1136. (a) The high resolution $12.6'' \times 10.0''$ $\mathtt{robust} = -0.5$ image shows the sources associated with the newly discovered filaments (detailed in Table 5): (A) WISEA J233615.95−313534.4 (B) WISEA J233616.55−313609.3 and (C) WISEA J233616.10−313741.1 labelled together with the radio bright head-tail galaxy PKS 2333−318. The contour levels in red start at $2\sigma = 80\,\mu$Jy beam^{-1} and scale by a factor of $\sqrt{2}$ to 750 μJy beam^{-1}. (b) shows the $25.5'' \times 21.3''$ low resolution $\mathtt{robust} = +2.0$ image of the same sources, plus the diffuse cluster emission. The contour levels in blue start at $2\sigma = 220\,\mu$Jy beam^{-1} and scale by a factor of $\sqrt{2}$ to 750 μJy beam^{-1}. The contour levels in red are the same as Figure 1a. The diffuse emission component, excluding point sources, was measured at 4.88 mJy$\pm$ 0.50; see § 3.2.1 and Table 3.

Table 3. Integrated flux densities and spectral indices of the Abell S1136 emission components. The flux densities of the filaments and diffuse regions (and their one-sigma uncertainties) were measured using NoiseChisel, as described in Section 3.2. These errors do not account for systematic errors (generally 10%). No spectral index is given for the filaments as the ATCA measurements may be affected by missing short spacings.

Source	$S_{154\,\mathrm{MHz}}$	$S_{185}\,\mathrm{MHz}$	$S_{215}\,\mathrm{MHz}$	$S_{888}\,\mathrm{MHz}$	$S_{2100}\,\mathrm{MHz}$	Spectral index (α)
			(mJy)			
Northern Filament	—	—	—	2.43 ± 0.11	0.20 ± 0.08	—
BCG Filament	—	—	—	1.94 ± 0.10	0.11 ± 0.07	—
Southern Filament	—	—	—	0.92 ± 0.07	0.11 ± 0.05	—
'Green' Diffuse Region[a]	—	—	—	4.88 ± 0.50	—	—
Box Total[b]	455.7 ± 6.5	260.3 ± 8.5	114.4 ± 16.6	18.9 ± 1.3	—	$-1.68^{+0.22c}_{-0.19}$

[a] The green diffuse region is shown in Figure 2(a).
[b] The box totals have been calculated within the cyan box shown in Figure 2(c). This includes both diffuse emission and discrete sources.
[c] The spectral index measurement also includes both diffuse and discrete sources, and as discussed in the text is probably flatter than the emission from the diffuse emission alone.
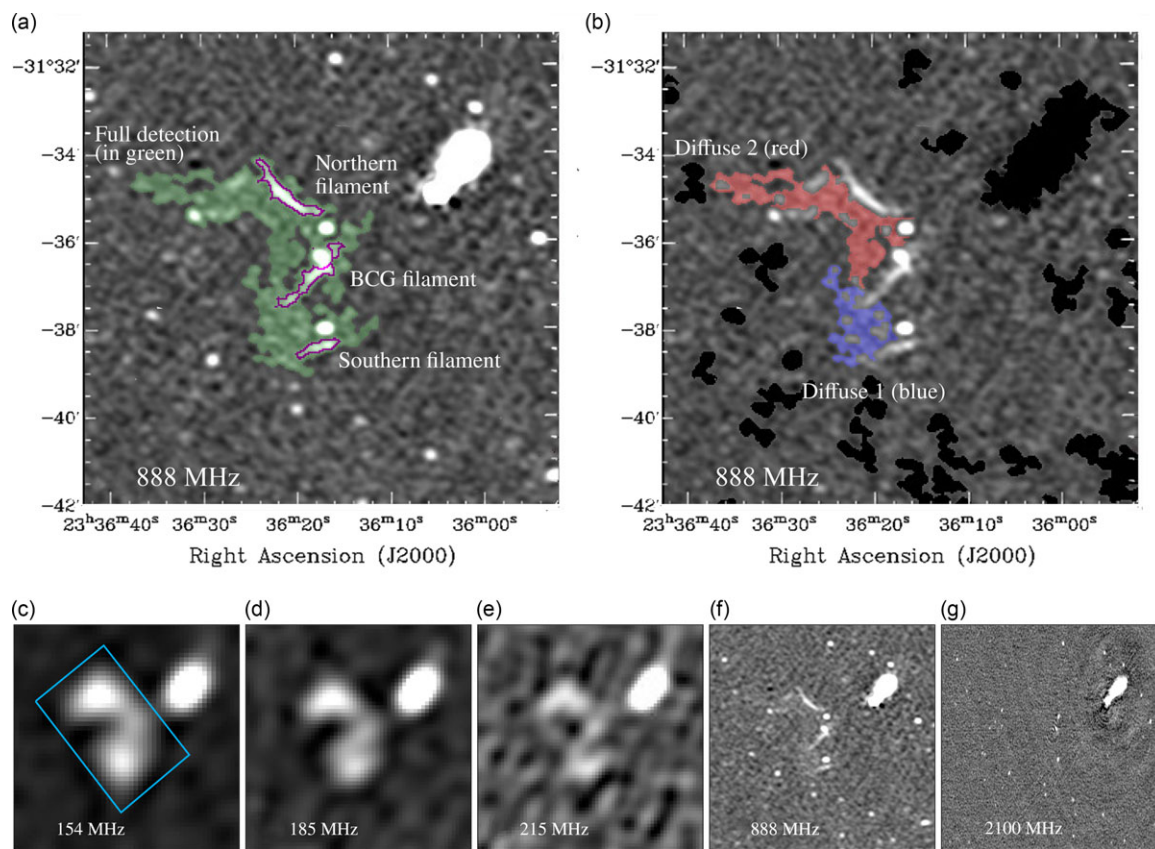
Figure 2. Detections in the galaxy cluster Abell S1136. (a) ASKAP 888 MHz ($12.6'' \times 10.0''$). The green region shows the NoiseChisel-detected region (9.7σ). The purple outline regions show the pixels within each filament using a 100 µJy beam^{-1} cut-off. (b) ASKAP 888 MHz (12.6×10.0 arcsec^2). The diffuse region is manually divided into the blue and red regions (Diffuse 1 and Diffuse 2) to measure the significance of the detection in them (6.6σ and 7.1σ, respectively). Other putative detections in the image at the same level are shown as black pixels, demonstrating that there are no other regions in the image with similar extended and contiguous emission. (c) to (g) show the images obtained by each telescope at the frequency shown. (c),(d),(e) are from MWA 2 with resolutions at $74.0'' \times 72.8''$, $62.5'' \times 61.6''$, and $53.9'' \times 53.7''$; (f) is from ASKAP ($12.6'' \times 10.0''$, and (g) is from ATCA ($6.31'' \times 3.05''$). The blue box in figure (c) is the region in which the total emission is measured, in order to exclude any contribution from PKS 2333−318.

Figure 2(b). We found a significance of 6.6σ and 7.1σ for the blue and red regions, respectively. The results of all measurements are shown in Table 3.

3.2.2. Total flux density

The total integrated flux density measurements for the cluster were obtained using images at all frequency bands, shown

Figure 2(c−g). In the lowest resolution MWA 2 image at 154 MHz, the galaxy cluster Abell S1136 and the head-tail radio galaxy PKS 2333−318 are the only significant radio detections. To measure the integrated spectral index of Abell S1136, we defined a region, shown as a cyan box in Figure 2(c), to exclude the emission from PKS 2333−318 and contain only the emission from Abell S1136. For the other frequencies (185, 215, 888, and 2100 MHz) we measured the integrated flux density within the same box. The

resulting integrated flux densities and spectral index are shown in Table 3.

3.3. Spectral index

A low-resolution spectral index map was produced using `robust = 0` images from MWA 2 at 154, 185, and 215 MHz, and ASKAP at 888 MHz. The data were regridded to the finest pixel grid (ASKAP 888 MHz $12.6'' \times 10.0''$) and convolved to the largest beam (MWA 2 154 MHz $73.95'' \times 72.85''$). The images were then stacked together, with the individual pixels in the stacked images processed through a simple weighted linear regression algorithm, with the slope of the best line of fit saved to a new image and output as a fits file. This image is shown in Figure 4. It is important to note that the resolution of the low frequency measurements does not allow the separation of the spectral index of the diffuse emission from that of the compact sources.

The MWA integrated flux measurements at 154, 185, and 215 MHz (see Table 3 and Figure 3), show a clear indication of a very steep spectrum $\alpha \sim -3.88$ component at low frequencies. Inclusion of the 888 MHz ASKAP integrated flux flattens the overall measured spectral index to $\alpha \sim -1.68$, shown by the solid black line in Figure 3. This is consistent with a steep-spectrum diffuse component which dominates at low frequencies but is faint at high frequencies, combined with a number of flatter-spectrum compact sources which dominate the total flux density at high frequencies, helping to flatten the spectral index fit. It is therefore difficult to determine if the diffuse emission alone is consistent with a power-law spectrum (van Weeren et al., 2019).

3.4. X-ray data

Figure 5 shows the X-ray image of Abell S1136 from observations with the XMM-Newton X-ray telescope (Id 0765041001) obtained as part of the extremely expanded HIghest X-ray FLUx Galaxy Cluster Sample (eeHIFLUGCS) follow-up project (Reiprich, 2017; Ramos-Ceja et al., 2019; Migkas et al., 2020; Pacaud et al. in prep.).

The data were processed and calibrated using the standard XMM-SAS processing tools (version 18.0.0). The calibrated eventlists were filtered for possible particle flare contamination based on a Poisson distribution fit to the [0.3-10.0] keV light curve values in time bins of 52/26s (resp. for the MOS/PN detectors). Time bins with count arrival rates outside the 3σ central range of the Poisson distribution were excluded as contaminated. This resulted in the exclusion of only 9% of the total exposure time. The instrumental background for each XMM-Newton (XMM)/EPIC exposure was modelled based on Filter Wheel Closed observations rescaled using the signal observed in the unexposed CCD corners. Images were extracted in the [0.5-2.0] keV band, resulting in the instrumental background subtracted, exposure corrected surface brightness map displayed in Figure 5. The morphology of the X-ray map confirms the emission peak to be coincident with the BCG defined at the coordinates in the ASKAP observations. The BCG is often associated with the geometric and kinematic galaxy centre, as well as the peak of the cluster X-ray emission (Lin & Mohr, 2004; Hudson et al., 2010).

Some features are further visible in the map that connects to the radio emission; (a) a possible excess coincident with the BCG filament, seen as a bright ridge which extends along the BCG radio emission, and (b) a possible 'channel' of missing thermal plasma
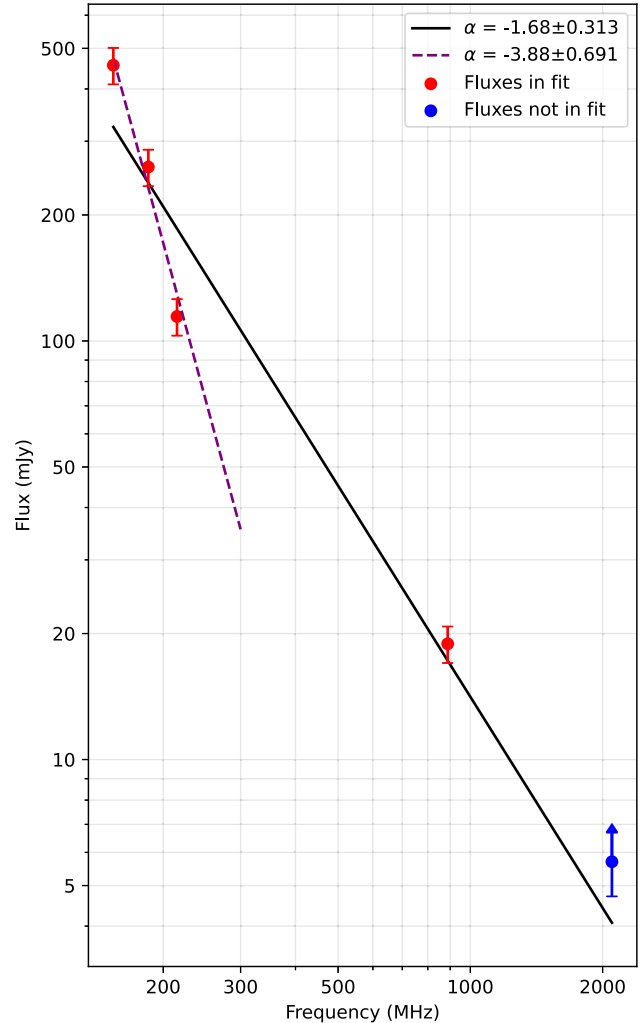

Figure 3. The spectral index measurements using the integrated flux of the diffuse emission and compact components in the Abell S1136 galaxy cluster. The flux measurements from Table 3 have been weighted and plotted with error bars derived from a quadrature sum of estimated 10% systematic errors plus the errors from Table 3. The solid black line shows the fit between MWA 154, 185, and 215 MHz, and ASKAP 888 MHz, with a spectral index of $\alpha \sim -1.68$. The ATCA 2100 MHz spectral index is plotted in blue and shown here as a lower limit. As described in Section 2.3, the ATCA flux is not included in the fit as the short spacings are not sensitive to the extended diffuse emission in Abell S1136. There is indication of a very steep spectrum component at low frequencies in the three MWA data points, with a spectral index of $\alpha \sim -3.88$. This is consistent with a steep-spectrum diffuse component which dominates at low frequencies, but is faint at high frequencies. Including both compact sources and diffuse emission means there are a number of flatter-spectrum compact sources which dominate the total flux density, helping to flatten the spectral index; particularly at higher frequencies.

at the position of the northern filament, shown by the yellow rectangle in Figure 5. We discuss this further in Section 4.2.

3.4.1. X-ray temperature and spectral profile analysis

To perform a more detailed spectroscopic analysis of the X-ray data, and measure other X-ray properties, we created a mask of the X-ray point sources to be excluded from the analysis. We first modelled the sky background from the outer regions of the pointing assuming that it consists of a contribution from the unresolved AGN population (an absorbed power-law spectrum with an X-ray spectral index of 1.46), the emission from the Milky Way halo
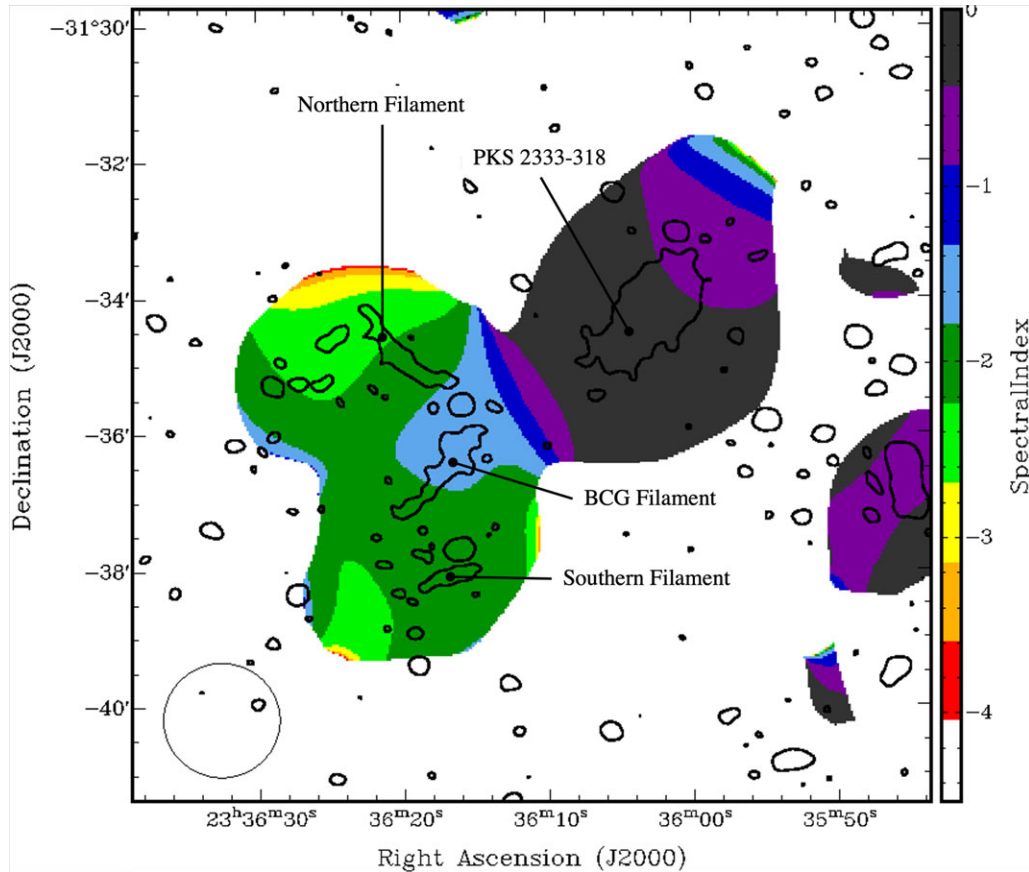
Figure 4. The spectral index map of the galaxy cluster Abell S1136. The map was created using images from MWA 2 @ 154 MHz ($74.0'' \times 72.8''$), 185 ($62.5'' \times 61.6''$) MHz, and 215 MHz ($53.9'' \times 53.7''$), and ASKAP 888 MHz ($12.6'' \times 10.0''$). Contours in black are at 100 μJy beam^{-1} from the ASKAP 888 MHz image. The data were regridded to the finest pixel grid and convolved to the largest beam. The MWA 2 beam is shown in the bottom left corner.

(an absorbed Astrophysical Plasma Emission Code (APEC) thermal model with solar metal abundance and a fitted temperature of ∼0.2 keV) and that of the local hot bubble (again absorbed solar metalicity APEC, with a temperature ∼0.1 keV). Our spectral modelling relied on version 3.0.9 of the APEC model and a fixed hydrogen column density of 1.23×10^{20} cm^{-2} derived from the Leiden/Argentine/Bonn (LAB) survey (Górski et al., 2005; Kalberla et al., 2005; Land & Slosar, 2007). Then we proceeded with extracting and modelling spectra in regions of interest, adding a further cluster APEC component to the area-rescaled sky background.

The red and grey points in Figure 6(b) show the average cluster temperature estimated in apertures of increasing size. The dashed line shows the average $R_{500} - T$ relation for a cluster at $z = 0.062$, based on the galaxy cluster mass-temperature (M−T) relation of Arnaud et al. (2005). The average temperature of the Abell S1136 galaxy cluster at the R_{500} radius of 8.4′ is ∼ 1.82 keV, shown by the intersection of the dashed and red lines in Figure 6(a). This enables us to estimate an approximate cluster R_{500}/M_{500} (the halo mass M_{500} out to a radius R_{500} within which the total mass density is 500 times the critical density of the Universe). Other cluster average properties are estimated from a direct fit to spectra extracted within R_{500} and shown in Table 4.

We note that the values shown in Table 5 differ slightly from the earlier ROSAT measurements (Migkas et al., 2020; Piffaretti et al., 2011) because (a) the ROSAT data include contributions

from AGN such as PKS 2333−318, and (b) the ROSAT temperature is based on data in the radius range $0.2 − 0.5 \times R_{500}$ (i.e. excluding the central 2′) whereas ours is based on all the emission within R_{500}.

Because the cluster shows a central surface brightness peak, and seems to be in a relatively relaxed state, we calculated a projected temperature and abundance profile to see if there is a cool core. The X-ray temperature profile is shown in red and grey in Figure 6(b).

3.5. Optical and infrared properties

We show the radio contours overlaid on a WISE image in Figure 7, and in Table 5 we list photometry and spectroscopy for sources A, B and C from the SkyMapper (Onken et al., 2019) and WISE (Wright et al., 2010) surveys, and the 2dF Galaxy Redshift Survey (De Propris et al., 2002). We classified the galaxies using WISE colours following the WISE colourcolour diagram (Wright et al., 2010).

Source A in Figure 1(a), located near the south-west end of the Northern Filament, is detected in both infrared (WISEA J233615.95−313534.4) and optical (SkyMapper J233615.95−313534.4). The WISE colours for this source (W1−W2 = −0.049, W2−W3 = 0.746) indicate this is most likely an elliptical galaxy. The redshift for this source is $z = 0.063 \pm 0.002$, so it is a cluster member.
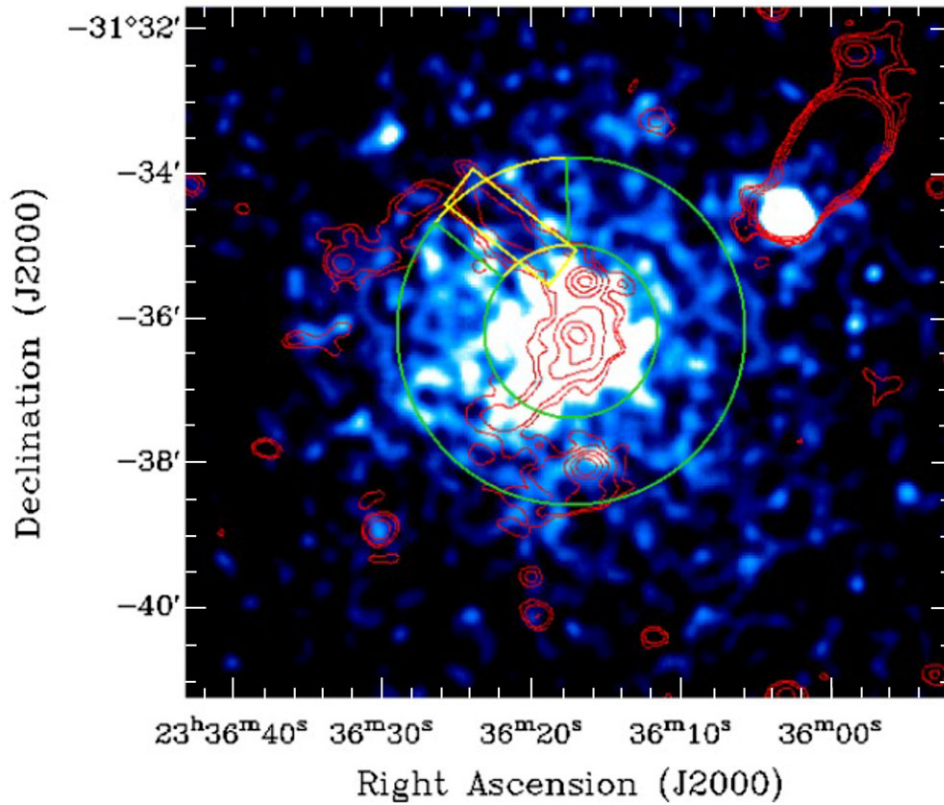
Figure 5. XMM-Newton X-ray image ($0.5-2$ keV) of the galaxy cluster Abell S1136 convolved to ASKAP 888 MHz low resolution image (Figure 1(b); $25.51'' \times 21.27''$), showing an X-ray peak located at RA(J2000) $= 23^h 36^m 16.54^s$ DEC(J2000) $= -31°36'09.''5$, coincident with the radio emitting BCG ESO 470-G020. ASKAP contours (red) are at 0.1, 0.15, 0.3, 0.6, and 1.0 mJy beam^{-1}. PKS 2333−318 (to the north-west of the cluster centre) is well within the projected extent of the Abell S1136 galaxy cluster ICM. The yellow rectangle (30'' wide) indicates a possible 'channel' of marginal ($\sim 4.3\sigma$) significance. The statistical significance of the channel was calculated using emission between 1 and 2' of the cluster centre (indicated by the inner and outer green rings) but excluding the region delineated by the two radial green lines, as described in Section 4.2.
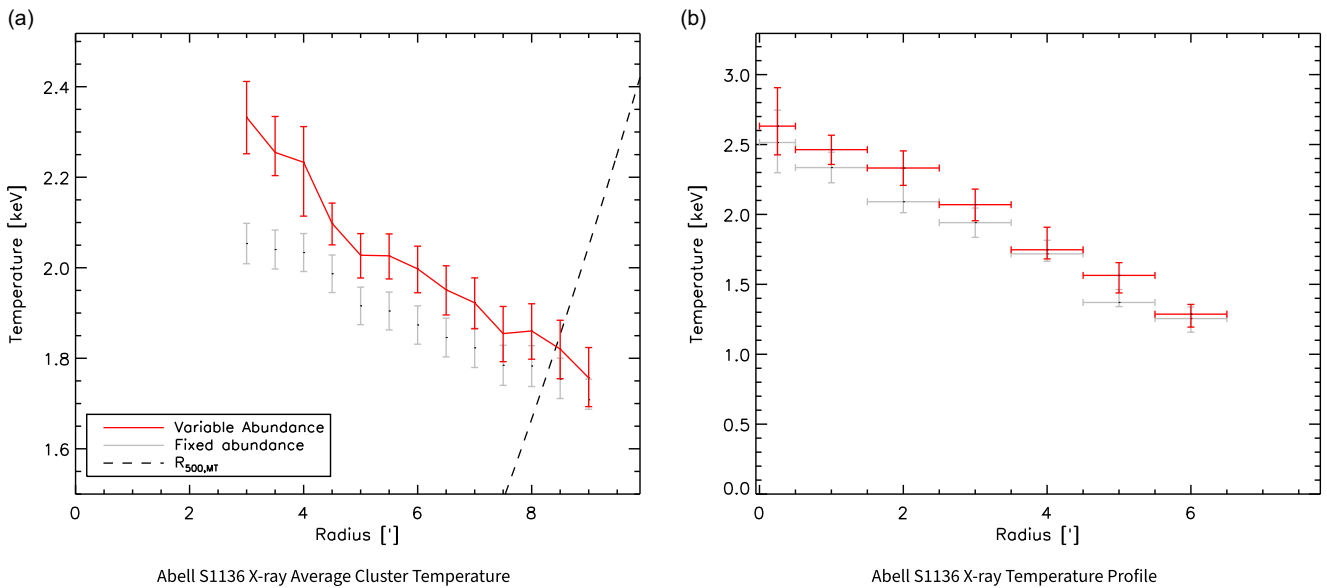
Figure 6. The X-ray temperature profiles of the Abell S1136 galaxy cluster; in both Figures the red line is the result leaving the metal abundance free, the grey line is for a fixed value of 0.3 solar. The location on the x-axis on both plots is the radial distance from the BCG at which the measurement is taken. Figure 6(a) shows the average cluster temperature (expressed as kT), estimated in apertures of increasing size from the cluster centre. The dashed line shows the average $R_{500} - T$ relation for a cluster at $z = 0.062$, based on the galaxy cluster mass-temperature (M−T) relation of Arnaud et al. (2005). The average temperature of the Abell S1136 galaxy cluster at 8.4' (the R_{500} radius) is ~ 1.82 keV, shown by the intersection of the dashed and red lines in Figure 6(a). Figure 6(b) shows the Abell S1136 X-ray temperature profile, with the cluster temperature plotted against radial distance in arcminutes from the cluster centre. The temperature profile appears linear from the centre to the edge, with no drop in temperature towards the cluster centre.
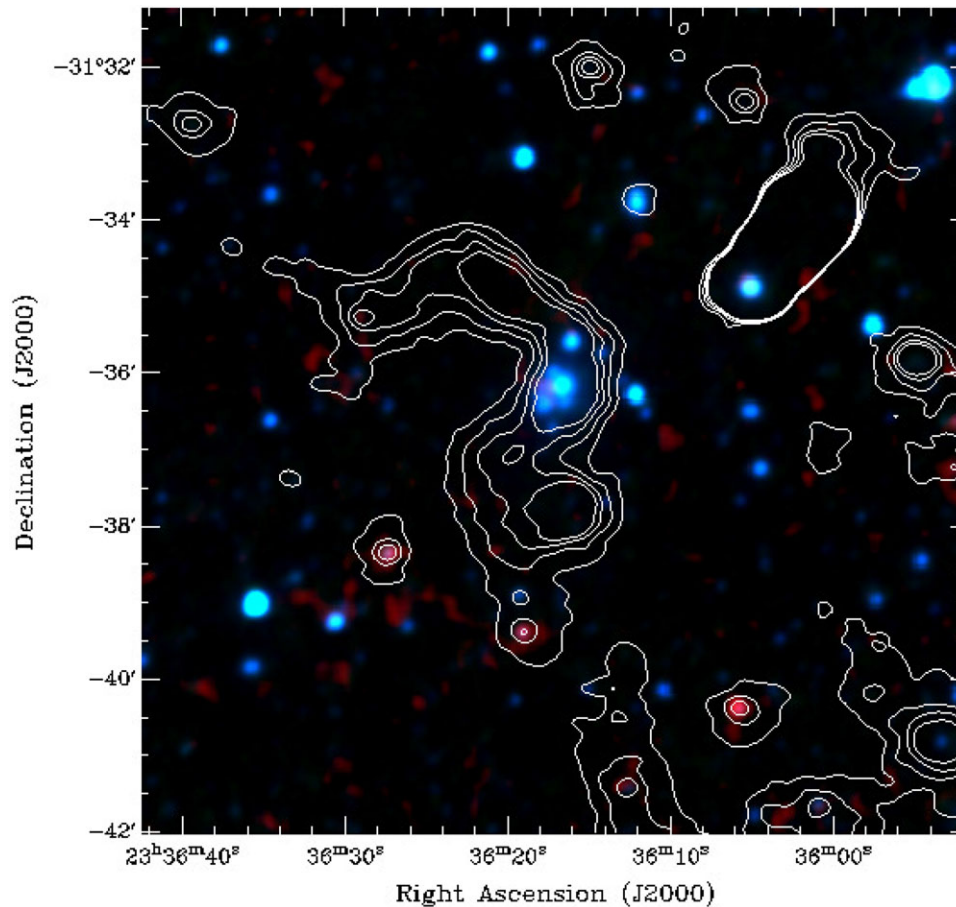
Figure 7. WISE infrared RGB image of the galaxy cluster Abell S1136, overlaid with radio contours from the ASKAP low resolution image (Figure 1b; 25.51″×21.27″). The RGB colours are red = 22μm, green = 4.6μm, blue = 3.4μm. The BCG ESO 470−G020 stands out near the image centre.

Table 4. The Abell S1136 average properties, as determined from the analysis of the XMM data. For the luminosities, the X-ray band (in keV) is indicated by the range in subscript.

Size	
R_{500}	(8.43′)
Total mass	
M_{500}	6.664 (+0.401/-0.399) 10^{13} M_ M$_\odot$
w. int. sc.	6.664 (+1.259/-1.543) 10^{13} M_ M$_\odot$
ICM quantities within R_{500}	
T_{spec}	1.826 (+0.063/-0.065) keV
Z	0.362 (+0.049/-0.044) $Z_\odot$
$L_{0.5-2.0}$	1.913 (+0.036/-0.036) 10^{36} W
$L_{0.1-2.4}$	3.165 (+0.073/-0.074) 10^{36} W
L_{bol}	4.300 (+0.077/-0.077) 10^{36} W

Source B in Figure 1(a) is the BCG of the Abell S1136 galaxy cluster and is coincident with the BCG Filament. This source is detected in both infrared (WISEA J233616.55−313609.3) and optical (SkyMapper J233616.52−313609.0). The WISE colours for this source (W1−W2 = −0.053, W2−W3 = 0.512) indicate this is most likely an elliptical galaxy. The redshift $z = 0.0622 \pm 0.0031$ for the Abell S1136 galaxy cluster is measured on this source.

Source C in Figure 1(a), located slightly above the Southern Filament, is detected as a faint source in WISE bands W1 and W2 but not in other optical or IR photometry, giving little indication of the nature of this source, and no redshift is available.

3.6. PKS 2333–318

The radio loud cluster member PKS 2333−318 lies to the north-west of the Abell S1136 galaxy cluster at RA(J2000) = 23^{h}36^{m}04.96^s DEC(J2000) = −31°34′51.″3. The redshift of PKS 2333−318 is $z = 0.06134$ (Jones et al., 2009). PKS 233−318 has an unusual single fat tail pointing away from the cluster centre. We consider this most likely to be a head-tail radio galaxy in which the jets have been blown back and merged by the ICM. There is evidence of subtle sub-structure as shown in Figure 8, although there is no clear evidence of the double tail often seen in a head-tail galaxy.

4. Discussion

Duchesne et al. (2021) detected diffuse emission from Abell S1136 using the MWA. While they say the diffuse emission could be categorised as a cluster halo, potential alternative interpretations include the presence of a cluster relic obstructing the line of sight towards the cluster, or the possibility of a dormant radio galaxy that might have previously been associated with the BCG, ESO

Table 5. Properties of the Infrared and Optical Sources near the three Abell S1136 Filaments.

Source	Source ID	Flux Density	Magnitude								Redshift
(Figure 1(a))		ASKAP (mJy)†	SkyMapper				WISEA				(z)*
			g	r	i	z	W1	W2	W3	W1-W2	
A	WISEA J233615.95−313534.4	1.24	16.197	15.617	15.135	14.845	12.396	12.445	11.699	−0.049	0.0630
	(SkyMapper J233615.95−313534.4)	±0.248	±0.010	±0.023	±0.022	±0.021	±0.023	±0.024	±0.249		±0.0021
B	WISEA J233616.55−313609.3	1.28	14.861	14.229	13.841	13.748	11.912	11.965	11.453	−0.053	0.0622
	(SkyMapper J233616.52−313609.0)	±0.256	±0.128	±0.091	±0.087	±0.133	±0.023	±0.023	±0.187		±0.0031
C	WISEA J233616.10−313741.1	1.51	−	−	−	−	16.049	15.648	12.716	0.401	−
		±0.302					±0.061	±0.128	(upper limit)		

† 20% uncertainty (Norris et al., 2021).
* Redshift from 2dFGRS (De Propris et al., 2002).
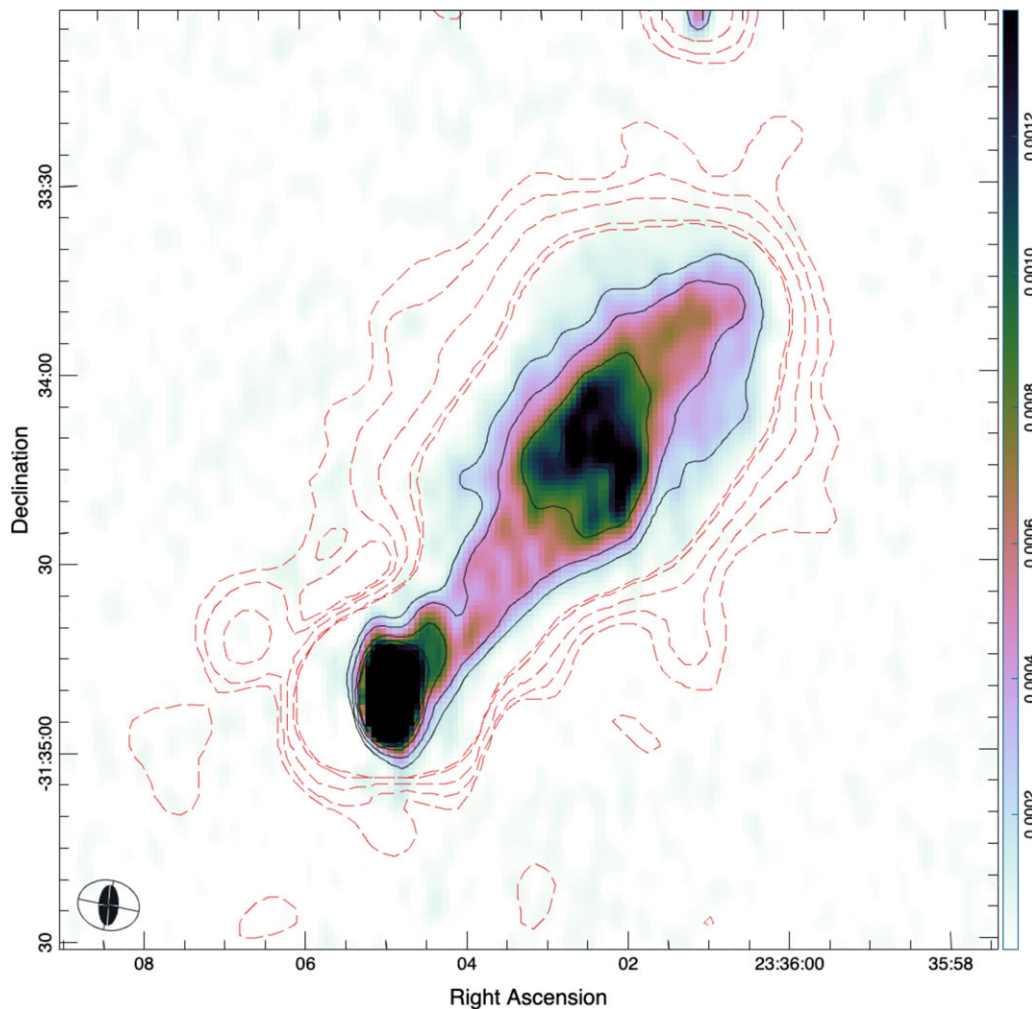
Figure 8. ATCA 2100 MHz radio continuum image (6.31″×3.05″) of the interesting head-tail galaxy PKS 2333−318, located to the north-west of the Abell S1136 galaxy cluster BCG. The solid black contours at 200, 400, 800, 1200, and 1600 μJy beam^{-1}, from the ATCA 2100 MHz image, outline the inner structure of the radio loud single tail emitted from PKS 2333−318. The dashed red contours, at 80, 160, 320, 640, and 750 μJy beam^{-1}, are from the ASKAP `robust = −0.5` image (12.6″×10.0″) shown in Figure 1(a). The ATCA and ASKAP beams are shown in the bottom left corner as a solid and open ellipses, respectively.

470−20. With the higher resolution and sensitivity of ASKAP (Figure 1(a), we now see that the diffuse emission detected with the MWA consists of several components: (a) a cloud of diffuse emission about 450 kpc in extent; (b) three filaments of emission; and (c) a number of compact sources, one of which we identify as the BCG.

4.1. The diffuse radio emission

The diffuse emission (shown in green in Figure 2(a)) is about 450 kpc in extent. We consider whether the diffuse emission can be attributed to a radio halo, which is typically ~ 700 kpc to ~ 1 Mpc in size and found in disturbed clusters (Chon et al., 2012; Chon & Böhringer, 2017), or to a mini-halo which is typically smaller; measuring less than 500 kpc in size, and found in relaxed clusters.

Radio halos are probably caused by electrons accelerated by turbulence in the wake of cluster collisions. They are extended in size and trace the presence of cosmic rays and magnetic fields in the ICM, and are seen in many merging galaxy clusters (see e.g. van Weeren et al., 2019). However, both the mass and the X-ray luminosity of the Abell S1136 galaxy cluster as reported here lie below any reported clusters with a radio halo (see eg Figure 9 in van Weeren et al. (2019)).

Radio mini-halos are normally found at the centre of relaxed cool-core clusters, and are associated with a radio galaxy that injects the electrons into the ICM. Mini-halo sizes extend to ~ 200 kpc from the central AGN, with some evidence of radial radial spectral steepening as seen in the Perseus cluster (Gitti et al., 2002), Abell 2626 (Gitti et al., 2004), and Ophiucus (Murgia et al., 2010). However, the higher sensitivity of the latest generation radio surveys is finding that many 'mini'-halos are far more extended than previously thought, with sizes up to approximately 0.5 Mpc; approaching the linear scales more commonly found for standard radio halos (e.g. Savini et al., 2018, 2019; Biava et al., 2021; Riseley et al., 2022a, 2023, 2024).

In Section 3.4, we showed that Abell S1136 has some properties expected for relaxed clusters, but with no evidence of a cool core. The X-ray and radio emission were found to be coincident with the centre of the galaxy cluster, located on the BCG ESO 470−20 (Lauberts & Valentijn, 1989).

The radio halo of a relaxed cluster classically consists of a smooth volume-filling region of radio emission that roughly follows the mass distribution of the cluster, and the radio halo centroid is coincident with the centroid of the X-ray emission, usually with some form of radial symmetry. The diffuse radio emission in Abell S1136, while roughly centred on the BCG and on the centroid of the X-ray emission, is far from being a contiguous or symmetric smooth region about the BCG.

The measured spectral index ($\alpha \sim -1.68$) of the diffuse emission in Abell S1136 is typical for radio halos or their smaller mini-halo counterparts ($\alpha < -1$). Revived fossil plasma sources often show steep spectral indices ($\alpha \lesssim -2$), and a curved spectrum (Riseley et al., 2022b); we see in Figure 3 the MWA 2 data at low frequencies exhibits a possible break in the simple power law fit, with the spectral index being steeper at the lower frequencies.

Although there might be a curved spectrum in the diffuse emission of the Abell S1136 galaxy cluster, as seen in revived fossil plasma, we are unable to quantify this as there are no measurements between the MWA 215 MHz and ASKAP 888 MHz data points. Therefore, the properties of the diffuse emission do not fit well with either classifications of a giant, or mini, radio halo.

We therefore cannot classify the source as a halo or mini-halo, and defer its classification to the wider discussion of the classification of diffuse emission from clusters (Govoni et al., 2019; Botteon et al., 2020; Knowles et al., 2022), prompted by higher resolution and sensitivity observations using telescopes such as ASKAP, MeerKAT, and LOFAR.

4.2. The X-ray channel

Figure 5 shows marginal evidence of a 'channel' through the hot gas of the ICM, coincident with the Northern filament. To calculate the statistical significance of this channel, we define a control region (shown in Figure 5) consisting of an annulus between 1 and 2′ around the cluster centre, excluding a region immediately surrounding the potential channel. We then fit a radial power law to the flux distribution inside the control annulus, corrected for various small effects, on which we simulate the channel using a MCMC (Markov chain Monte Carlo) with 50 million points. This resulted in an estimated probability of obtaining the observed channel by chance that corresponds to $\sim 4.3\sigma$, which we regard as 'marginally significant'. We therefore acknowledge that this channel may just be a statistical fluctuation in the noise. For example, other similar 'holes' in the X-ray surface brightness can be seen in Figure 5, possibly due to the intrinsic variance of the underlying ICM distribution. Furthermore, there is no evidence for an overall anti-correlation between radio and X-ray. However, the alignment with the radio is curious, and therefore merits some discussion. If this channel is real, it might be caused by the interaction of the radio jet from an AGN with the hot X-ray gas in the ICM. Examples of this have been seen in NGC 1275 (Boehringer et al., 1993), (Rudnick et al., 2022b) and possibly in Abell S0102 (Read et al., 2001; Filipovic et al., 2010). However, it is unclear whether the radio emission in the current case is confined by the X-ray medium, with the X-ray gas guiding the radio emission, or is the result of a channel being bored by the radio jet (Jones et al., 2017) through the hot gas. In either case, the filament would then presumably represent a radio jet from source A. However, we are cautious about over-interpreting this channel as it is of marginal statistical significance (4.3 σ).

4.3. Filaments

Filamentary radio emission in clusters is typically caused by radio shocks, as discussed in Section 1, and are typically aligned tangentially around the periphery of the cluster (van Weeren et al., 2019); With the possible exception of the Southern Filament, the three filaments that we have identified in the Abell S1136 do not follow this pattern. In some cases the filamentary emission can be at the periphery of the cluster, but seen in projection – eg along the line of sight through the cluster, so the periphery is facing us; this might be the case for the Southern Filament.

The Northern Filament is ∼140 kpc long and is oriented towards the radio galaxy A, which is at a similar redshift to the BCG galaxy B. As discussed above in Section 4.2, there is marginal evidence for an X-ray channel coincident with this filament, suggesting the filament may represent a fossil radio jet from source A. Alternatively, since the filament is near the periphery of the cluster, it could be a radio shock.

The BCG filament appears to extend from the BCG and is ∼140 kpc long. This is most likely to be a fossil jet associated with galaxy B, although we cannot discount the possibility that it might be a section of an unusual WAT.

The Southern Filament is only ∼80 kpc long, and may be associated with with radio source C, in which case it might be revived fossil plasma. However, the filament is perpendicular to the radius vector from the BCG, suggesting that it may be a radio shock. No

redshift is available for the radio source C, and therefore we do not know whether or not this source is associated with the cluster.

With new deep and high resolution low-frequency observations, such as as upgraded Giant Metrewave Radio Telescope (uGMRT) and MeerKAT, the existence, morphology, and spectral nature of these filaments could be confirmed and studied in more detail. Additionally, deep linear polarisation data such as from the ASKAP Polarisation Sky Survey of the Universe's Magnetism (POSSUM; Gaensler et al., 2010) could reveal the polarisation fraction and orientation of the magnetic fields which may help discern whether these are shocks are not.

4.4. X-ray

In our analysis of the X-ray temperatures in the Abell S1136 cluster, we do not see cooler emission in the central parts, which would be characteristic of a cool core cluster (Hudson et al., 2010). Instead the central parts appear significantly hotter, which would indicate either that the cluster is not relaxed, or that the central AGN inside the BCG also emits X-rays, which would harden the spectra. However, we found no evidence for AGN emission. The reduced χ^2 for the spectral modelling of the central bin is not changed significantly by adding a power-law component to account for a central AGN, which does not allow us to dismiss or confirm this hypothesis. However, we note that the best fit AGN contribution would be 10% of the central flux and would flatten the central profile to temperature values comparable to the measurements at $0.2-0.3\ R_{500}$, which is more in line with expectations for a cluster without evidence for a strong merger event. It would also explain quite well the central surface brightness peak in a cluster without a cool core.

5. Conclusions

The diffuse radio emission in the Abell S1136 galaxy cluster appeared in earlier observations to be an amorphous radio blob, similar in appearance to a radio halo.

Our higher-resolution and higher-sensitivity ASKAP observations show that it breaks up into: (a) a region of diffuse emission about 450 kpc in extent; (b) three filaments located within the diffuse emission, each $80-140$ kpc in extent; and (c) a small number of compact radio sources. The diffuse emission shows some structure which was not evident in earlier low-resolution observations, and its properties do not closely match either those of a halo or mini-halo. However, the distinction between halos and mini-halos is becoming less clear in other high-sensitivity observations of clusters.

The three filaments appear similar to those increasingly being found in high-sensitivity observations of other cluster sources, although we cannot rule out the possibility that they represent an unusual WAT. Further investigation using higher quality spectral index data and polarisation information would be helpful.

Our X-ray analysis of Abell S1136, based on XMM-Newton observations, shows a distinctive X-ray emission pattern closely aligned with the radio emission from the BCG. This alignment reinforces the BCG's role as both the geometric centre and the locus of the cluster's X-ray emission. There is a possible 'channel' in the X-ray plasm, which aligns with the 'Northern' filament; however evidence for the channel is only marginally significant at 4.3σ. While it is interesting, it may just signify a statistical fluctuation. The X-ray temperature profile shows that the cluster appears to be in a relaxed state, with no evidence of a cool core.

We note that these filaments, and the structure in the diffuse emission, were not visible in earlier, low-resolution observations, and we speculate that many cluster radio sources which are currently regarded as smooth extended sources may well show more complex structure, such as that we see in Abell S1136, when observed with next-generation radio telescopes such as ASKAP, MeerKAT, uGMRT and LOFAR. The wealth of such details that we can expect in the next few years may prompt a re-examination of the classifications of the radio properties of clusters that have been based on low-resolution data.

available from the corresponding authors upon reasonable request. Catalogue information was obtained from SkyMapper[j] and VizieR[k].

The code to reproduce the NoiseChisel results in Section 3.2.1 is available at https://gitlab.com/makhlaghi/abell-s1136.

References

Akhlaghi, M. 2019a, arXiv e-prints, arXiv:1909.11230

Akhlaghi, M. 2019b, in Astronomical Society of the Pacific Conference Se- ries, Vol. 521, Astronomical Data Analysis Software and Systems XXVI, ed. M. Molinaro, K. Shortridge, & F. Pasian, 299

Akhlaghi, M., & Ichikawa, T. 2015, ApJS, 220, 1

Arnaud, M., Pointecouteau, E., & Pratt, G. W. 2005, A&A, 441, 893

Beardsley, A. P., Johnston-Hollitt, M., Trott, C. M., et al. 2019, PASA, 36, e050

Biava, N., de Gasperin, F., Bonafede, A., et al. 2021, MNRAS, 508, 3995

Biava, N., Bonafede, A., Gastaldello, F., et al. 2024, arXiv e-prints, arXiv:2403.09802

Bock, D. C. J., Large, M. I., & Sadler, E. M. 1999, AJ, 117, 1578

Boehringer, H., Voges, W., Fabian, A. C., Edge, A. C., & Neumann, D. M. 1993, MNRAS, 264, L25

Bonafede, A., Feretti, L., Murgia, M., et al. 2010, A&A, 513, A30

Bonafede, A., Intema, H. T., Bruggen, M., et al. 2014, MNRAS, 444, L44

Botteon, A., van Weeren, R. J., Brunetti, G., et al. 2020, MNRAS, 499, L11

Botteon, A., Shimwell, T. W., Cassano, R., et al. 2022, A&A, 660, A78

Bowman, J. D., Cairns, I., Kaplan, D. L., et al. 2013, PASA, 30, e031

Brentjens, M. A. 2008, A&A, 489, 69

Briggs, D. S. 1995, PhD thesis, The New Mexico Institute of Mining and Technology

Brunetti, G., Cassano, R., Dolag, K., & Setti, G. 2009, A&A, 507, 661

Campusano, L. E., Marinello, G., Clowes, R. G., et al. 2018, ApJ, 869, 145

Carilli, C. L., & Taylor, G. B. 2002, ARA&A, 40, 319

Cassano, R., Gitti, M., & Brunetti, G. 2008, A&A, 486, L31

Chon, G., & Böhringer, H. 2017, A&A, 606, L4

Chon, G., Böhringer, H., & Smith, G. P. 2012, A&A, 548, A59

Clarke, T. E., Kronberg, P. P., & Böhringer, H. 2001, ApJ, 547, L111

Comrie, A., Wang, K.-S., Hsu, S.-C., et al. 2021, CARTA: The Cube Anal- ysis and Rendering Tool for Astronomy, doi: 10.5281/zenodo.3377984

Condon, J. J., Cotton, W. D., Greisen, E. W., et al. 1998, AJ, 115, 1693

Cuciti, V., Cassano, R., Brunetti, G., et al. 2021a, A&A, 647, A50

Cuciti, V., Cassano, R., Brunetti, G., et al. 2021b, A&A, 647, A51

De Propris, R., Couch, W. J., Colless, M., et al. 2002, MNRAS, 329, 87

Donnert, J., Vazza, F., Brüggen, M., & ZuHone, J. 2018, Space Sci. Rev., 214, 122

Duchesne, S. W., Johnston-Hollitt, M., ORringa, A. R., et al. 2021, PASA, 38, e010

Duchesne, S. W., Johnston-Hollitt, M., Zhu, Z., Wayth, R. B., & Line, J. L. B. 2020, PASA, 37, e037

Ensslin, T. A., Biermann, P. L., Klein, U., & Kohle, S. 1998, A&A, 332, 395

Feretti, L., Giovannini, G., Govoni, F., & Murgia, M. 2012, A&A Rev., 20, 54

Filipovic, M. D., Crawford, E. J., Jones, P. A., & White, G. L. 2010, Serbian Astronomical Journal, 181, 31

Filipović, M. D., & Tothill, N. F. H. 2021, Principles of Multimessenger Astronomy (IOP Publishing), doi: 10.1088/2514-3433/ac087e

Frater, R. H., Brooks, J. W., & Whiteoak, J. B. 1992, Journal of Electrical and Electronics Engineering Australia, 12, 103

Gaensler, B. M., Landecker, T. L., Taylor, A. R., & POSSUM Collaboration. 2010, in American Astronomical Society Meeting Abstracts, Vol. 215, American Astronomical Society Meeting Abstracts #215, 470.13

Ghirardini, V., Eckert, D., Ettori, S., et al. 2019, A&A, 621, A41

Giacintucci, S., Venturi, T., Macario, G., et al. 2008, A&A, 486, 347

Giovannini, G., & Feretti, L. 2004, Journal of Korean Astronomical Society, 37, 323

Giovannini, G., Tordi, M., & Feretti, L. 1999, New A, 4, 141

Gitti, M., Brunetti, G., Feretti, L., & Setti, G. 2004, A&A, 417, 1

Gitti, M., Brunetti, G., & Setti, G. 2002, A&A, 386, 456

Gitti, M., Tozzi, P., Brunetti, G., et al. 2015, in Advancing Astrophysics with the Square Kilometre Array (AASKA14), 76

Gooch, R. 1995, Astronomical Society of the Pacific Conference Series, Vol. 77, Space and the Spaceball (Astronomical Society of the Pacific), 144

Górski, K. M., Hivon, E., Banday, A. J., et al. 2005, ApJ, 622, 759

Govoni, F., Orrù, E., Bonafede, A., et al. 2019, Science, 364, 981

Guzman, J., Whiting, M., Voronkov, M., et al. 2019, ASKAPsoft: ASKAP science data processor software, ascl:1912.003

Hindson, L., Johnston-Hollitt, M., Hurley-Walker, N., et al. 2014, MNRAS, 445, 330

Hotan, A. W., Bunton, J. D., Chippendale, A. P., et al. 2021, PASA, 38, e009

Hudson, D. S., Mittal, R., Reiprich, T. H., et al. 2010, A&A, 513, A37

Hurley-Walker, N., Payne, J. L., Filipović, M. D., & Tothill, N. 2021, in Multimessenger Astronomy in Practice: Celestial Sources in Action, ed. M. D. Filipović & N. F. H. Tothill (IOP Publishing), 2–1

Jaffe, W. J. 1977, ApJ, 212, 1

Johnston, S., Bailes, M., Bartel, N., et al. 2007, PASA, 24, 174

Johnston, S., Taylor, R., Bailes, M., et al. 2008, ExA., 22, 151

Jones, D. H., Read, M. A., Saunders, W., et al. 2009, MNRAS, 399, 683

Jones, T. W., Nolting, C., O'Neill, B. J., & Mendygral, P. J. 2017, Phys. Plasmas, 24, 041402

Kalberla, P. M. W., Burton, W. B., Hartmann, D., et al. 2005, A&A, 440, 775

Kempner, J. C., Blanton, E. L., Clarke, T. E., et al. 2004, in The Riddle of Cooling Flows in Galaxies and Clusters of alaxies, ed. T. Reiprich, J. Kempner, & N. Soker, 335

Knowles, K., Cotton, W. D., Rudnick, L., et al. 2022, A&A, 657, A56

Land, K., & Slosar, A. 2007, Phys. Rev. D, 76, 087301

Lauberts, A., & Valentijn, E. A. 1989, The surface photometry catalogue of the ESO-Uppsala galaxies (Garching: European Southern Observatory)

Lin, Y.-T., & Mohr, J. J. 2004, ApJ, 617, 879

Mauch, T., Murphy, T., Buttery, H. J., et al. 2003, MNRAS, 342, 1117

McConnell, D., Allison, J. R., Bannister, K., et al. 2016, PASA, 33, e042

McConnell, D., Hale, C. L., Lenc, E., et al. 2020, PASA, 37, e048

Migkas, K., Schellenberger, G., Reiprich, T. H., et al. 2020, A&A, 636, A15

Murgia, M., Eckert, D., Govoni, F., et al. 2010, A&A, 514, A76

Nelson, G. J. 1992, J. Electr. Electron. Eng. Aust., 12, 113

Norris, R. P., Hopkins, A. M., Afonso, J., et al. 2011, PASA, 28, 215

Norris, R. P., Marvil, J., Collier, J. D., et al. 2021, PASA, 38, e046

Offringa, A. R., Trott, C. M., Hurley-Walker, N., et al. 2016, MNRAS, 458, 1057

Olowin, R. P. 1988, PASP, 100, 1354

Onken, C. A., Wolf, C., Bessell, M. S., et al. 2019, PASA, 36, e033

Ozawa, T., Nakanishi, H., Akahori, T., et al. 2015, PASJ, 67, 110

Pasini, T., Edler, H. W., Brüggen, M., et al. 2022, A&A, 663, A105

Paul, S., Kale, R., Datta, A., et al. 2023, JApA, 44, 38

Piffaretti, R., Arnaud, M., Pratt, G. W., Pointecouteau, E., & Melin, J. B. 2011, A&A, 534, A109

Pizzo, R. F. 2011, JApA, 32, 567

Rajpurohit, K., Hoeft, M., Wittor, D., et al. 2022, A&A, 657, A2

Ramos-Ceja, M. E., Pacaud, F., Reiprich, T. H., et al. 2019, A&A, 626, A48

Read, A. M., Filipović, M. D., Pietsch, W., & Jones, P. A. 2001, A&A, 369, 467

Reiprich, T. 2017, in The X-ray Universe 2017, ed. J.-U. Ness & S. Migliari, 189

Riseley, C. J., Rajpurohit, K., Loi, F., et al. 2022a, MNRAS, 512, 4210

Riseley, C. J., Bonnassieux, E., Vernstrom, T., et al. 2022b, MNRAS, 515, 1871

Riseley, C. J., Biava, N., Lusetti, G., et al. 2023, MNRAS, 524, 6052

Riseley, C. J., Bonafede, A., Bruno, L., et al. 2024, arXiv e-prints, arXiv:2403.00414

Rudnick, L., Brüggen, M., Brunetti, G., et al. 2022a, ApJ, 935, 168

Rudnick, L., Brüggen, M., Brunetti, G., et al. 2022b, ApJ, 935, 168

Sault, R. J., Teuben, P. J., & Wright, M. C. H. 1995, in Astronomical Soci- ety of the Pacific Conference Series, Vol. 77, Astronomical Data Analysis Software and Systems IV, ed. R. A. Shaw, H. E. Payne, & J. J. E. Hayes, 433

[i] https://wiki.mwatelescope.org/display/MP/Data+Access
[j] http://skymapper.anu.edu.au/
[k] https://vizier.u-strasbg.fr/viz-bin/VizieR

Savini, F., Bonafede, A., Brüggen, M., et al. 2018, MNRAS, 478, 2234

Savini, F., Bonafede, A., Brüggen, M., et al. 2019, A&A, 622, A24

Slee, O. B., Roy, A. L., Murgia, M., Andernach, H., & Ehle, M. 2001, AJ, 122, 1172

Stroe, A., Sobral, D., Röttgering, H. J. A., & van Weeren, R. J. 2014, MNRAS, 438, 1377

Thompson, A. R., Moran, J. M., & Swenson, GEORGE W., J. 2017, Interferometry and Synthesis in Radio Astronomy, 3rd Edition (Springer International Publishing AG), doi: 10.1007/978-3-319-44431-4

Tingay, S. J., Goeke, R., Bowman, J. D., et al. 2013, PASA, 30, e007

Tümer, A., Wik, D. R., Zhang, X., et al. 2023, ApJ, 942, 79

van Weeren, R. J., de Gasperin, F., Akamatsu, H., et al. 2019, Space Sci. Rev., 215, 16

van Weeren, R. J., Hoeft, M., Röttgering, H. J. A., et al. 2011, A&A, 528, A38

van Weeren, R. J., Röttgering, H. J. A., Brüggen, M., & Hoeft, M. 2010, Science, 330, 347

van Weeren, R. J., Brunetti, G., Brüggen, M., et al. 2016, ApJ, 818, 204

Velović, V., Cotton, W. D., Filipović, M. D., et al. 2023, MNRAS, 523, 1933

Venturi, T., Bardelli, S., Dallacasa, D., et al. 2017, Galaxies, 5, 16

Wayth, R. B., Tingay, S. J., Trott, C. M., et al. 2018, PASA, 35, e033

Wilson, W. E., Ferris, R. H., Axtens, P., et al. 2011, MNRAS, 416, 832

Wright, E. L., Eisenhardt, P. R. M., Mainzer, A. K., et al. 2010, AJ, 140, 1868